



## Article

**Cite this article:** Karlsen T, Johansson M, Lohse J, Doulgeris AP (2024). Incidence angle dependency and seasonal evolution of L and C-band SAR backscatter over landfast sea ice. *Annals of Glaciology* **65**, e29, 1–14. <https://doi.org/10.1017/aog.2024.30>

Received: 29 April 2024

Revised: 9 July 2024

Accepted: 5 August 2024

**Keywords:**


Arctic glaciology; remote sensing; sea ice; sea-ice geophysics

**Corresponding author:**

Truls Karlsen;

Email: [truls.t.karlsen@uit.no](mailto:truls.t.karlsen@uit.no)

# Incidence angle dependency and seasonal evolution of L and C-band SAR backscatter over landfast sea ice

Truls Karlsen , Malin Johansson , Johannes Lohse  and Anthony P. Doulgeris 

UiT The Arctic University of Norway, Tromsø, Norway

**Abstract**

We estimate sea-ice type specific incidence angle (IA) dependencies for dual polarized (HH/HV) L and C-band synthetic aperture radar (SAR) for the winter, melt onset and advanced melt seasons for level and deformed ice, using time-series of Advanced Land Observing Satellite-2 (ALOS-2) and Sentinel-1 imagery off the north-east coast of Greenland. The IA dependencies are used to radiometrically correct the L and C-band backscatter time-series, which enables analysis of their seasonal evolution. From this, we observe that the L-band backscatter intensity increases for both ice types at the transition from winter to melt onset. We use these results to estimate ice type separability and to train an IA aware Bayesian classifier at both frequencies. These results show that while both frequencies are capable of distinguishing level and deformed ice during the winter, only L-band SAR can reliably make this separation during the melt onset season. During the advanced melt season, the overall classification accuracies are similarly low for L and C-band. This study demonstrates the potential of L-band SAR for sea-ice mapping, which is highly relevant in the light of several upcoming L-band SAR missions.

**1. Introduction**

With diminishing sea-ice extent in the Arctic Ocean (Meier and Stroeve, 2022) and a growing demand for marine operations, an increase in shipping activity is seen (Lasserre and Pelletier, 2011; Stephenson and others, 2013; Lasserre and Tétu, 2020). Operational sea-ice mapping is currently performed manually by trained ice analysts using predominantly (wide-swath) synthetic aperture radar (SAR) imagery, though this approach is subjective and time consuming. Computer-assisted ice type mapping shows potential, e.g. Malmgren-Hansen and others (2020); Wang and others (2023); however, automated ice type classification based on SAR C-band imagery is challenging when the melt season starts as the wet snow masks out the backscatter contribution from the ice (Onstott and Carsey, 1992). L-band SAR can potentially mitigate this problem, as the longer wavelength is less susceptible to the rapidly changing snow conditions during the melting season (Onstott and Carsey, 1992; Casey and others, 2016).

Wide-swath SAR imagery is most commonly used for ice charting because of its broad spatial coverage. The incidence angle (IA) increases continuously across the swath width and the radar backscatter intensity generally decreases with increasing IA. However, the rate of the decrease depends on the scattering properties of the surface and inner structure of the medium imaged, where the contribution from the latter depends on the penetration depth (Casey and others, 2016). When the backscatter intensity is given in decibel (dB), its decrease can be approximated by a linear function for the typical IA range of wide-swath SAR imagery (Cristea and others, 2020). The rate of decrease is then also referred to as the ‘slope’ and is typically given in dB per 1°. Slopes for different sea-ice types have been well studied for C-band data, particularly during the winter season (Mäkynen and others, 2002; Mäkynen and Karvonen, 2017; Mahmud and others, 2018; Aldenhoff and others, 2020), with a thorough summary of C-band slopes given in a recent study by Geldsetzer and Howell (2023). In their work, the authors investigated the IA dependency of C-band sea-ice backscatter for both the winter and melt season using successive image differencing to estimate the IA dependency from Radarsat Constellation Mission (RCM) data. The advantage of this method is that by using successive scenes from a time-series with high temporal resolution, the impact of changing physical properties in the sea ice and snow cover is reduced. This is of particular importance during the melt season, when physical changes in the snow and ice properties occur more rapidly than during the cold winter season.

Investigations of the IA dependency for L-band backscatter over sea ice are more sparse. A summary of L-band slopes from previous studies is given in Table 1. Note that Mahmud and others (2018) is the only study that provides ice type specific IA dependencies. Apart from Karvonen and others (2020), these studies were limited to the winter season and only considered the IA dependency for the HH polarization. Karvonen and others (2020) estimated general sea-ice slopes for both HH and HV polarization for the period January–August. It should be noted that the Advanced Land Observing Satellite-2 (ALOS-2) data used in their study were acquired before a change in the settings of the HV-channel was applied (11 April 2018), after which the performance over ocean and coastal regions improved Aldenhoff and others (2018).

© The Author(s), 2024. Published by Cambridge University Press on behalf of International Glaciological Society. This is an Open Access article, distributed under the terms of the Creative Commons Attribution licence (<http://creativecommons.org/licenses/by/4.0/>), which permits unrestricted re-use, distribution and reproduction, provided the original article is properly cited.

[cambridge.org/aog](https://cambridge.org/aog)



**Table 1.** Previous studies on the IA dependency of sea-ice backscatter from L-band SAR (FYI = First Year Ice, MYI = Multi Year Ice)

Channel	Ice type	Slope [dB/1°]	Period	Region	Satellite	Source
HH	Unspecified	−0.25	February – March	Canadian Arctic Archipelago (CAA)	ALOS	Mahmud and others (2018)
	FYI	−0.21				
	MYI	−0.30				
HH	Unspecified	−0.246	January	Kara and Barents seas Arctic Ocean (North of Svalbard)	ALOS-2	Karvonen and others (2020)
HV	Unspecified	0.085	– August			
HH	Unspecified	−0.25	March – May			

Wakabayashi and others (2004), while not providing slope estimates, found that for L-band SAR the HH-channel backscatter monotonically decreased with increasing IA for thin ice, smooth ice, and rough ice, while the HV-channel showed no IA dependency for these classes. The HV-channel backscatter values were, however, at the same level as the system noise floor in their study, hence the IA dependency of the cross-pol channel at L-band requires further investigation.

Incorporating per-class IA dependencies in classification algorithms has been shown to improve classification results for C-band SAR (Lohse and others, 2020; Cristea and others, 2020). We therefore use IA dependencies and temporal backscatter evolution to train such a classifier at both L and C-band. While L-band ice type classification has been studied using fully polarimetric SAR data (Dierking, 2009; Dabboor and others, 2017; Singha and others, 2020), the use of wide-swath SAR data for this purpose has received less attention. Comparisons of L and C-band SAR backscatter over sea ice have been made by Mahmud and others (2018) for the winter season and by Casey and others (2016) for the melt season. The L-band SAR data in these studies were acquired by the Phased Array L-band Synthetic Aperture Radar (PALSAR) sensor onboard ALOS in ScanSAR Wide mode, and therefore contained only the HH-channel and covered a more limited IA range compared to ALOS-2 PALSAR-2 imagery. Toyota and others (2021) compared the capabilities of L and C-band SAR for separating level and deformed ice across different IAs using images from the Sea of Okhotsk. They concluded that L-band was more suitable for this task with accurate separation extending into the melt season. However, their study was limited to seasonal sea ice and hence a thinner ice regime consisting primarily of pancake ice, nilas and thin level ice. Their findings might therefore not be directly transferable to regions containing thicker, potentially heavily deformed ice covers, which may be encountered in the Arctic Ocean or Fram Strait region. Mahmud and others (2022) used overlapping C and L-band ScanSAR data to study both single- and multi-frequency ice type classification in the Canadian Arctic Archipelago (CAA) during the freeze-up season, though the case study was limited to two L and C-band image pairs and IA corrected co-polarized channel data. As such, more research on ice type classification from L-band wide-swath data is needed for different seasons and including multiple polarization channels. This is of particular importance in light of new and upcoming operational L-band missions such as NISAR, ALOS-4 PALSAR-3 and ROSE-L, which will provide wide-swath data suitable for operational sea-ice mapping.

In this study, we use a time-series of ALOS-2 PALSAR-2 (L-band) and Sentinel-1 (S1) (C-band) imagery over landfast sea ice off the north-east coast of Greenland lasting from November 2021 to August 2022 to estimate IA dependencies and evaluate the temporal evolution of backscatter intensities for different ice types. These findings are then used as input to train IA aware classifiers at both frequencies in order to compare

the performances of L and C-band for ice type mapping. The objectives of this study can be summarized as:

1. Estimate IA dependencies for both the HH and HV-channel at L and C-band for level and deformed ice throughout a full season;
2. Investigate the seasonal backscatter evolution for both frequencies for different ice types;
3. Use the above findings as input for IA aware classification for both L and C-band.

## 2. Study area and data

The study area is Belgica Bank, a region off the north-east coast of Greenland, which can be seen in Figure 1. The sea ice around Belgica Bank is both formed locally and advected from the Arctic Ocean. A large portion of the ice in the region is fast ice, as grounded icebergs and ridge keels lock the ice in place over the shallow bank (Vinje, 1986; Hughes and others, 2011). In this study, we focus on different ice types within the fast ice area at Belgica Bank. This allows us to easily monitor the same sea-ice surfaces in fixed regions of interest (ROIs) over time. Furthermore, it enables the direct comparison of observations at different frequency, even with time differences between the image acquisitions images of up to several days. Moreover, in April and May 2022, in situ data were collected within the study area and a weather buoy (AWI0801) was deployed (see section ‘In situ data’ for more details).

### 2.1 SAR data

We used SAR data acquired at both L-band (ALOS-2) and C-band (S1) from the period where the fast ice persisted (11 November 2021 to 1 August 2022). Both datasets consist of dual-polarized imagery (HH and HV), meaning that a horizontally (H) polarized radar signal was transmitted and was received by both a horizontally and vertically (V) oriented antenna. All available ALOS-2 ScanSAR scenes from descending orbits were used in this study. Ascending orbit scenes were available in the end of January and beginning of February, however, an unexplained shift in backscatter intensity was observed over the same location and IA between descending and ascending orbits. We therefore chose to disregard the scenes from ascending orbits to simplify the analysis. For the C-band data, we used all available S1 imagery from ascending and descending orbits acquired in extra wide-swath (EW) mode over the study area. The total number of scenes used was 47 ALOS-2 scenes and 220 S1 scenes. In addition, we used scenes from 2023 covering the same region as test data for the ice type classification, which consisted of an additional six ALOS-2 scenes and eight S1 scenes. A complete list of the ALOS-2 scenes used can be found in Appendix A (Table 7). Specifications of the sensor modes and data used are given in Table 2.

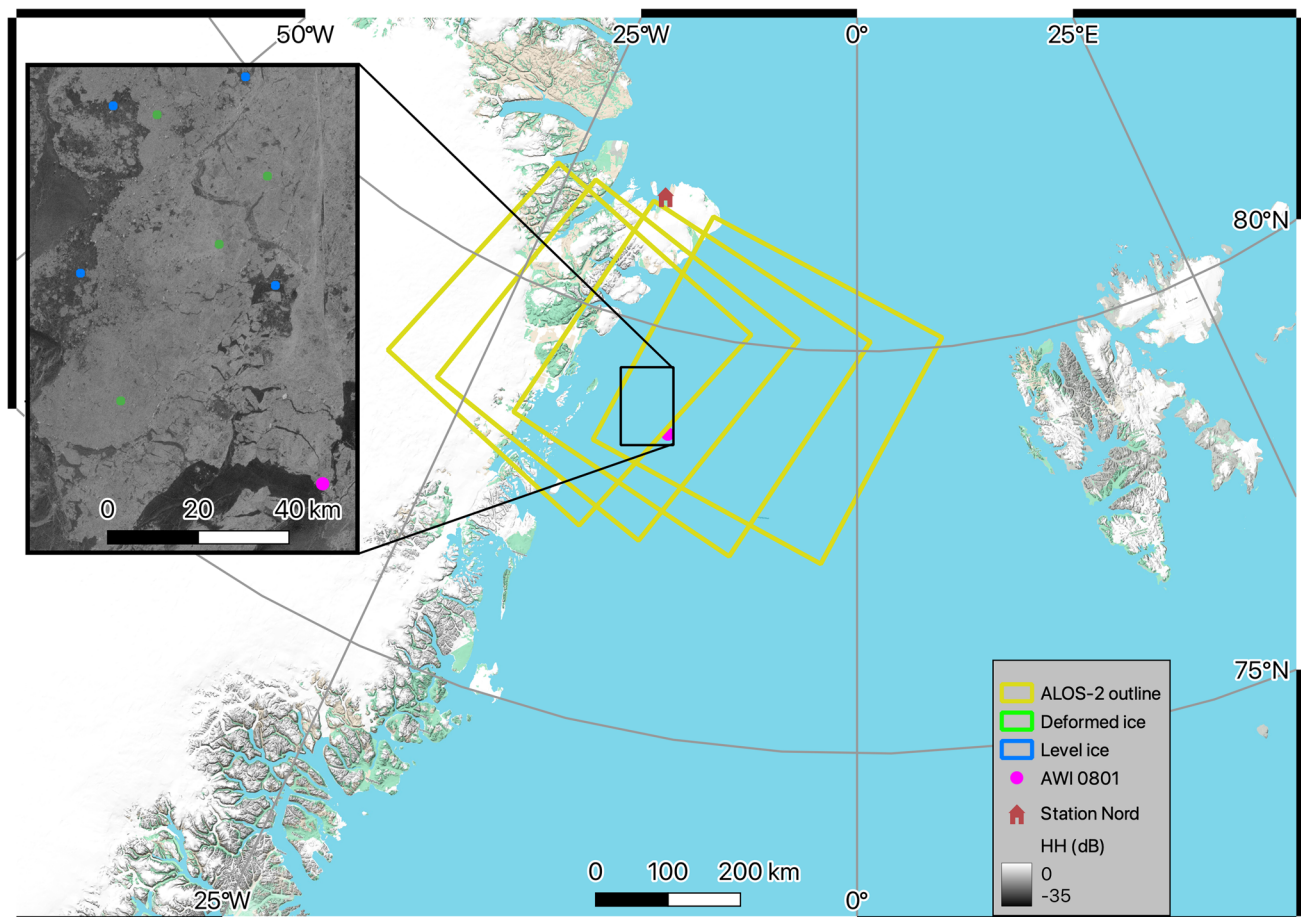


**Figure 1.** Map of the study area, with ALOS-2 scene outlines marked by yellow squares. The inset image is an ALOS-2 HH-channel image from 10/04/2022 calibrated to  $\sigma^0$  (dB). The blue and green regions are the ROIs for level and deformed ice, respectively. The location of the weather buoy *AWI0801* is marked by a pink circle, and the location of Station Nord is marked by an orange house. Map data: Google.

## 2.2 In situ data

We used temperature data collected by a sea-ice mass-balance array (SIMBA) buoy (Jackson and others, 2013) deployed in the fast ice (78.69° N, 12.07° W) during the CIRFA cruise 2022 (Dierking and others, 2022). Weather data from Villum research station at Station Nord, from here on referred to as Station Nord, were used to connect the temperature evolution with the backscatter evolution for the fast ice. The temperature records were used as a basis to define three different seasons: winter, melt onset and advanced melt.

The temperature data from the SIMBA buoy provide on-site measurements for the period 28 April 2022 to 13 July 2022 (Fig. 2). Temperature measurements were made by a 4.8 m long thermistor chain, with thermistors spaced 2 cm apart, initially measured with a sampling interval of 6 h, which was increased to 2 h from 24 May 2022 onwards (Dierking and others, 2022). The seven uppermost thermistors were placed above the ice and

are used as an estimate of the air temperatures in the region. The temperature measurements from the thermistors were averaged to produce one time-series, which was subsequently filtered with a running median filter of length seven to remove short timescale fluctuations.

We retrieved daily mean, minimum and maximum temperature records for the period 1 November 2021 to 1 August 2022 from Station Nord (81.60° N, 16.67° W) through the Danish Meteorological Institute (DMI) open data API (<https://opendata.docs.dmi.govcloud.dk/DMIOpenData>, accessed: 30 January 2024). The temperature time-series is shown in Figure 2, with three different seasons (see section 'Definition of seasons') highlighted by colors: orange for winter, gray for melt onset and red for advanced melt. Prior to snow/ice melting, which caused the SIMBA temperature profile to hover around 0° C, the Spearman's rank correlation coefficient between the SIMBA and Station Nord profiles was 0.68. Based on the similarity we deemed it reasonable to use the data from Station Nord as a proxy for the air temperatures at

**Table 2.** Specifications of the satellite data used in this study, spatial resolution is given as range x azimuth (NESZ = Noise Equivalent Sigma Zero)

Sensor	Mode	Pixel spacing	Swath width	IA range	NESZ (dB)	Spatial resolution
ALOS-2 <sup>a</sup> S1 <sup>d</sup>	ScanSAR Normal	25 × 25 m	350 km	25°–49°	–26	95.1 × 77.7 m <sup>b,c</sup>
	EW	40 × 40 m	410 km	18.9°–47°	–22	20 × 40 m

<sup>a</sup> <https://www.eorc.jaxa.jp/ALOS-2/en/about/palsar2.htm>, accessed: 06/11/2023

<sup>b</sup> <https://www.restec.or.jp/en/solution/product/product-alos-2/alos-2-about.html>, accessed: 18/04/2024

<sup>c</sup> With 5 looks in azimuth and 3 looks in range

<sup>d</sup> <https://sentinels.copernicus.eu/web/sentinel/user-guides/sentinel-1-sar/acquisition-modes/extra-wide-swath>, accessed: 17/01/2024



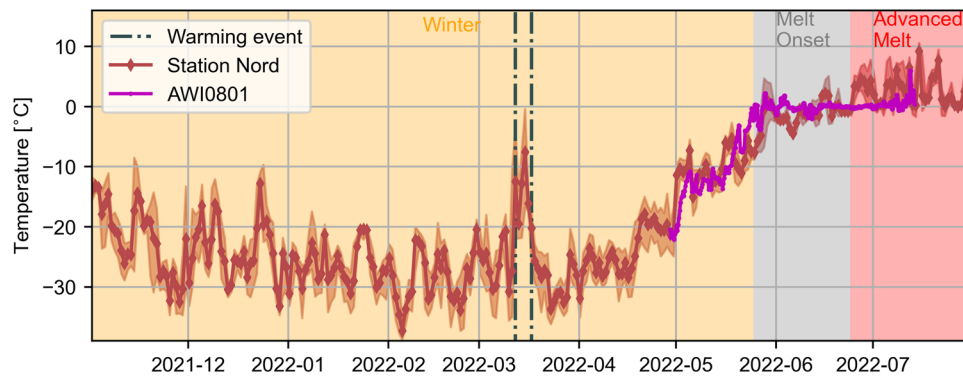


**Figure 2.** Temperature records from the SIMBA buoy *AWI0801* (magenta) and Station Nord (red). Daily mean, minimum and maximum from Station Nord are shown, with the solid line representing the mean temperature and the shaded area the span between the minimum and maximum temperatures. The background colors indicate the different seasons; winter (yellow), melt onset (gray) and advanced melt (red). A brief warming event was observed between 12 March 2022 and 17 March 2022, which is indicated by two dashed-dotted vertical dark gray lines.

Belgica Bank for the entire period, even though Station Nord is located  $\sim 330$  km north-west of the SIMBA buoy.

### 2.2.1 Definition of seasons

Based on the temperature records (Fig. 2) and assisted by interpretation of the C-band backscatter time-series, we separated the SAR data into three distinct seasons. Following the descriptions given by Barber and others (2001) and Casey and others (2016), we were able to define the following three seasons for this study: winter, melt onset and advanced melt. The first instance of positive temperatures from the on-site temperature measurements occurred on 25 May 2022, which we defined as the start of the melt onset season. Temperature observations from Station Nord stayed consistently above  $0^{\circ}\text{C}$  from 24 June 2022, which we determined to be the transition from melt onset to advanced melt. The melt onset and advanced melt seasons are represented by two clusters of ALOS-2 scenes, acquired during the periods 2 June 2022–6 June 2022 and 4 July 2022–1 August 2022, respectively. The acquisition frequency of S1 for the melt onset and advanced melt seasons was similar to the post S1-B failure winter season frequency (1–3 days between scenes).

Thorough descriptions of the evolution of C-band radar backscatter in different thermodynamic sea-ice regimes are given in Barber and others (2001) and Casey and others (2016). Barber and others (2001) provide the temporal evolution of C-band SAR backscatter for first-year ice (FYI) and multi-year ice (MYI), starting with the freeze-up in autumn and transitioning through winter, early melt, melt onset and advanced melt. The winter season is characterized by cold sea ice and dry snow, and subsequently stable SAR signals for both ice types. This extends into the early melt season, which is characterized by the onset of snow metamorphism. As such, small amounts of water may be present in the snow pack, though not enough to cause significant scattering at C-band and longer wavelengths. Barber and others (2001) observed that there was no discernible difference between the winter and early melt C-band SAR signals, as the amount of water present in the snow pack during melt onset was still small. This is in line with what we observed (see section ‘Analysis of temporal backscatter evolution’), and we therefore chose to group these two seasons together for our analysis. The transition from early melt to melt onset occurs when liquid water is consistently present in the snow pack. This increase in liquid water present in the snow pack reduces the penetration depth of the radar signal, which at C-band causes surface scattering from the wet air-snow interface and volume scattering from the snow to be the dominant scattering mechanism for both level and deformed ice. As such, separation of ice types becomes

difficult from C-band SAR during this period, however longer wavelengths could potentially penetrate deeper into the wet snow and still give a returned signal that partly originates from surface scattering at the snow-ice interface. (Barber and others, 2001; Casey and others, 2016; Mahmud and others, 2020). The transition from melt onset to advanced melt occurs when the snow pack is completely saturated by water, which is followed by rapid snow melt. During this period, the ice surface also experiences melting. The advanced melt period is also characterized by the formation of melt ponds, which depending on the wind conditions can cause a significant increase or decrease in SAR backscatter (Barber and others, 2001). However, as melt ponds are typically smaller in size than the spatial resolution of wide-swath SAR data, a mixture of melt ponds, wet snow and bare ice may be present within a pixel (Casey and others, 2016). As the advanced melt season progresses, pond drainage initiates which is followed by ice breakup (Barber and others, 2001).

## 3. Method

Here we describe the methodology used to (1) process the SAR data and estimate the IA dependency of sea ice, (2) estimate class separability for different frequencies and seasons, and (3) perform ice type classification at both L and C-band.

### 3.1 SAR processing

#### 3.1.1 Preprocessing

We applied precise orbits and thermal noise removal to the S1 data using the *Sentinel Application Platform* (SNAP) version 9.0.0. All SAR scenes (ALOS-2 and S1) were then calibrated to  $\sigma^0$  and multi-looked. To account for the difference in spatial resolution of the ALOS-2 and S1 data products (Table 2), we used different multi-looking windows:  $3 \times 3$  for ALOS-2 and  $2 \times 2$  for S1. We then projected the images to EPSG:3996 IBCAO Polar Stereographic with a pixel spacing of 80 m and converted the backscatter intensities to dB. We also extracted the IA information, which was resampled to match the pixel spacing of the calibrated SAR scenes before being projected to the same coordinate reference system.

#### 3.1.2 Selection of ROIs

Two different types of sea ice are investigated in this study, namely level and deformed sea ice. The class definition follows the classification scheme for the area in Lohse and others (2024); Færch and others (2024), but is limited to the classes that occur in the landfast area. Level ice is defined as ice with

no apparent large-scale deformation and a relatively smooth surface, which results in low backscatter intensity at both HH and HV polarization during cold and dry winter conditions, when the snow cover has minimal influence on the SAR signal. Deformed ice is ice that has undergone large-scale deformation resulting in ridges of meter scale or large rubble fields, which give a high backscatter intensity at both HH and HV polarization during winter conditions. In Lohse and others (2024), the classes are defined based on visual analysis of overlapping SAR and optical data, with the optical data confirming the presence (or absence) of large-scale deformation. Since ice age cannot be directly inferred on a pixel basis from such overlapping image pairs, no distinction is made between FYI or MYI. However, as the level ice is formed in-situ at Belgica Bank, it can easily be tracked back in time and is confirmed to be FYI. The deformed ice is advected from the north and likely consists of a mixture of MYI and deformed FYI. Operational ice charts from DMI (not shown) confirm that the fast ice area contains a mixture of deformed FYI and MYI, with an approximately equal amount of old ice (MYI) and thick FYI. The class definitions should be kept in mind when comparing the results from this study to those of previous work.

Based on visual interpretation of the SAR imagery, we manually selected ROIs for level and deformed ice in stable regions of the fast ice area using QGIS and the ALOS-2 HH-channel. Scenes acquired during the winter season were used to identify the ROIs, which were manually inspected to make sure the ROIs stayed within the fast ice for the period investigated. To avoid class contamination and mixed classes, the selected ROIs are relatively small, 1000 m in width and height, and located such that edges between different ice types are not contained within the ROIs. We selected four ROIs for each ice type. Examples of the selected regions are shown in Figure 3. Due to the stability of the fast ice area, the same ROIs can be used to study the temporal evolution of the backscatter signatures at both L and C-band. An overview of the range of IAs covered at L and C-band for both ice types during the different seasons is given in Table 3.

### 3.1.3 Estimation of IA dependence

We estimated IA dependency using successive image differencing, from here on referred to as the differencing method (Mäkynen and Karvonen, 2017; Geldsetzer and Howell, 2023). The IA

**Table 3.** Minimum and maximum IA covered by the selected ROIs at L and C-band for each season

Wavelength	Level ice		Deformed ice		Season
	Minimum	Maximum	Minimum	Maximum	
L-band	28.237°	48.829°	29.925°	48.340°	Winter
C-band	22.271°	45.857°	22.689°	45.393°	
L-band	28.275°	48.879°	28.967°	48.344°	Melt onset
C-band	27.945°	45.852°	28.545°	45.389°	
L-band	33.248°	48.899°	34.042°	48.356°	Advanced melt
C-band	27.934°	45.857°	28.534°	45.393°	

dependency is calculated by extracting the mean backscatter ( $\overline{\sigma^0}$ ) and IA ( $\overline{IA}$ ) within an ROI for two subsequent scenes, and estimating the backscatter slope coefficient as a function of IA as follows:

$$b = \frac{\overline{\Delta\sigma^0}}{\overline{\Delta IA}} \quad (1)$$

where  $b$  is the backscatter IA dependency. For the S1 time-series, we use two subsequent scenes in time to estimate the slope. The time-series of ALOS-2 scenes was significantly more sparse, so in order to obtain additional slope estimates, we utilized a pair-wise comparison between each ALOS-2 scene and the next three scenes in time. Time separations for ALOS-2 and S1 can be seen in Table 4. There were large time separations between some of the ALOS-2 scenes during the winter and advanced melt seasons, though no particular influence from this on the slope estimates could be observed and as such we did not introduce any time separation cut-offs. Slope estimates as a function of  $\overline{\Delta IA}$  for both L and C-band from the winter season can be seen in Figure 4,

**Table 4.** Mean, minimum and maximum time separation between scenes used for successive image differencing for ALOS-2 and S1 (Time separations for the three different seasons are provided for ALOS-2, while time separations for the periods with S1-A and -B and only S1-A are given for S1; d denotes day(s) while m denotes minutes)

	ALOS-2			S1	
	Winter	Melt onset	Advanced Melt	A + B	A
Mean	8.8 d	2.2 d	14 d	0.8 d	2.1 d
Min	1 d	2 d	2 d	48 m	0.4 d
Max	38 d	5 d	26 d	2 d	5 d

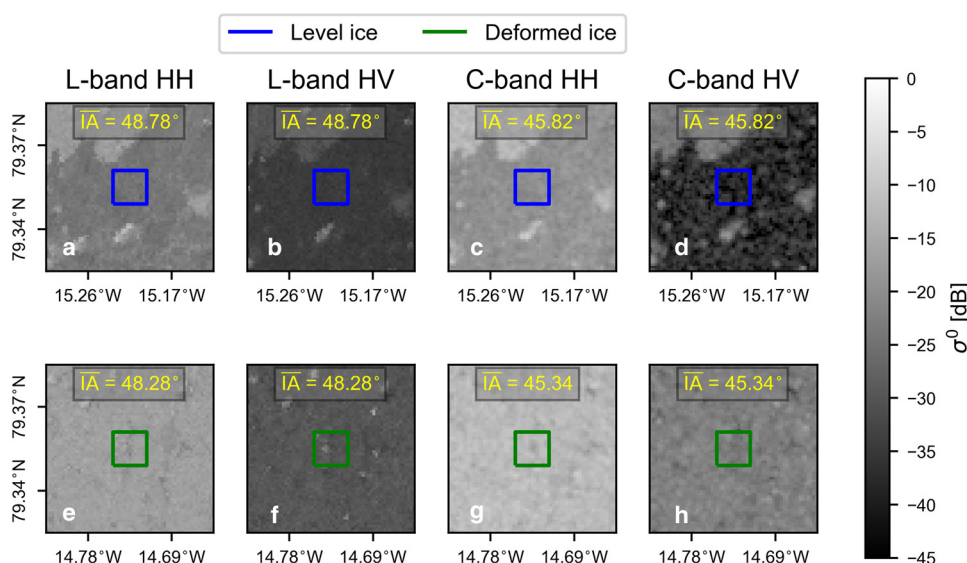


**Figure 3.** Examples of ROIs for level ice (blue, (a)–(d)) and deformed ice (green, (e)–(f)). The shown areas cover 5 × 5 km and the size of the ROIs is 1 × 1 km. The mean IA within each ROI is given in yellow. The SAR imagery is from 12 February 2022.

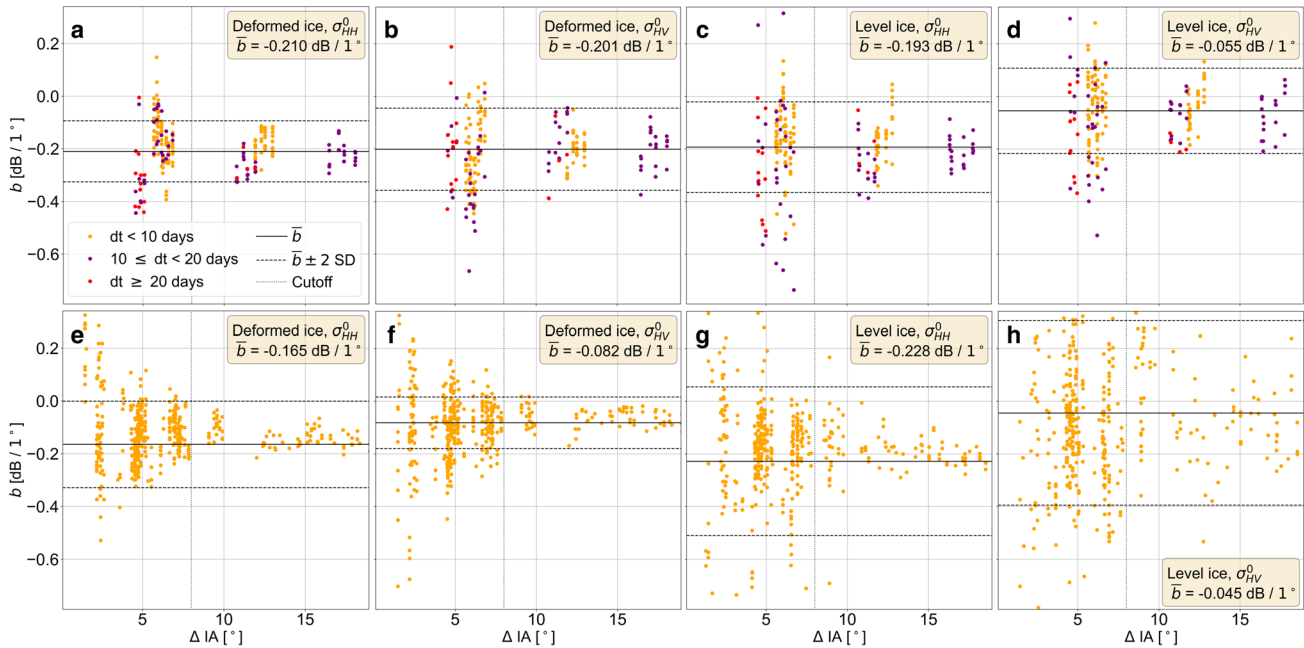


**Figure 4.** Slopes as a function of  $\Delta\bar{IA}$  during the winter season. L-band slopes for deformed ice HH (a), deformed ice HV (b), level ice HH (c) and level ice HV (d). C-band slopes for deformed ice HH (e), deformed ice HV (f), level ice HH (g) and level ice HV (i). The separation in time between two scenes used to estimate the slope is denoted as ‘dt’.

where the slope estimates are grouped by the time separation between the scenes used. The time separation between S1 scenes increased after the failure of S1-B (23 December 2021), but stayed consistent between seasons after this.

Similar to Geldsetzer and Howell (2023), we observe that small IA differences result in a larger spread of the slope estimates (Fig. 4). As all the ALOS-2 data were acquired from four repeating orbits, the slope estimates are grouped into three groups of similar  $\Delta\bar{IA}$ . Hence, there was a gap between  $\Delta\bar{IA} \approx 7^\circ$  and  $\Delta\bar{IA} \approx 11^\circ$  with no data points. We observed that the group from  $\Delta\bar{IA} < 7^\circ$  had large spread in the slope estimates, and we therefore chose a cutoff at  $\Delta\bar{IA}_{\text{cutoff}} = 8^\circ$ , which is similar to the cutoff used in Geldsetzer and Howell (2023). This cutoff was applied to the S1 data as well.

After discarding the slope estimates from below  $\Delta\bar{IA}_{\text{cutoff}}$ , we averaged the remaining slopes to produce a single slope estimate for each ice type at both channels during the different seasons at both frequencies. These slope estimates are used to correct the backscatter, and as input for the ice type classification algorithm. To generate the time-series of slopes (Fig. 5) the slope estimates from all ROIs for each day were averaged.

### 3.2 Class separability

To estimate class separability we used the Jeffries-Matusita (JM) distance, where a score of 2 indicates a perfect separability and a score of 0 indicates inseparable classes.  $JM > 1$  is therefore deemed to indicate ‘high’ separability while  $JM < 1$  indicates ‘low’ separability. We chose this method as it is computationally inexpensive and is well suited for classification of remote-sensing data (Sen and others, 2019). The JM distance requires the mean vector and covariance matrix of the classes as input. Since the mean vector is IA dependent and we have estimated the slopes, we replace the constant mean with a linearly variable mean and hence obtain class separability as a function of IA.

### 3.3 Ice type classification

We performed ice type classification with both L and C-band SAR data using a Bayesian classification approach with per-class IA

dependency developed by Lohse and others (2020). The ROIs used to estimate the IA dependencies were used as training data, where mean vectors, IA slopes and covariance matrices for each class at each band were estimated using both L and C-band data. We trained separate classifiers for each season at both L and C-band using the 2021–2022 data.

For validation of our classifier, we selected ROIs from images over the same area in 2023, making the validation dataset completely independent from the training dataset. The validation ROIs were extracted from three ALOS-2 and four S1 scenes from the winter season, two ALOS-2 and three S1 scenes from the melt onset season, and one scene from the advanced melt season for both sensors. We evaluated the classification performance on a per-scene basis using the per-class accuracy:

$$\text{Per-class accuracy} = \frac{\text{Total correctly classified from class X}}{\text{Total number of pixels from class X}} \quad (2)$$

where X is a given class, in this case level or deformed ice. We also used the overall accuracy (OA):

$$\text{OA} = \frac{\text{Total number of correctly classified pixels}}{\text{Total number of pixels}} \quad (3)$$

Both accuracy metrics were adapted from Stehman and Foody (2009).

## 4. Results and analysis

In this section, we present and analyze the IA dependencies, and use these findings to produce radiometrically corrected SAR backscatter time-series for both L and C-band, and to evaluate class separability at both L and C-band during the different seasons. Finally, we present and evaluate the classification results for the fast ice area for different seasons.

### 4.1 Seasonal IA dependency

We estimated the per-class IA dependency of each polarization channel at both L and C-band frequency for all three seasons.

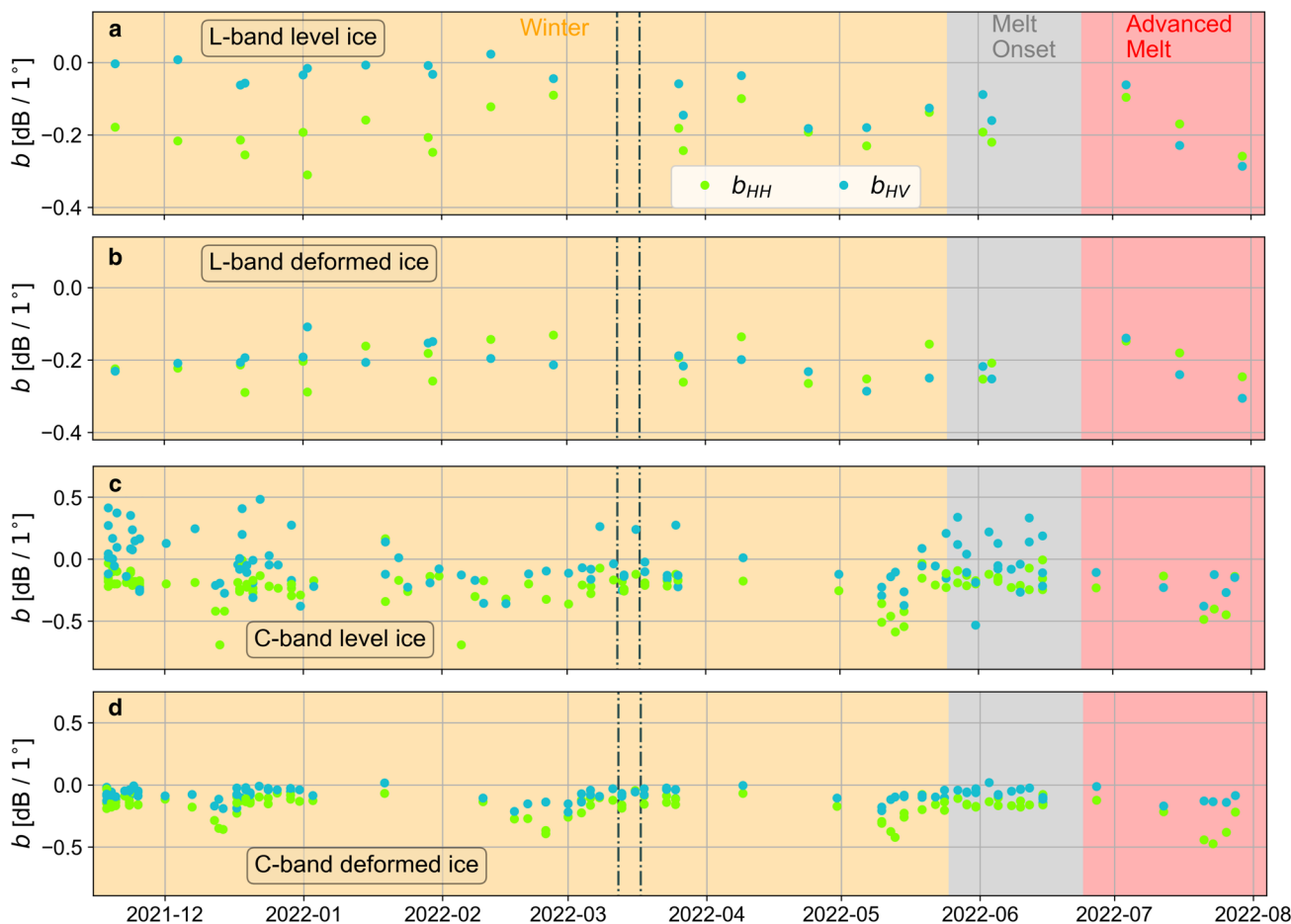


**Figure 5.** Time-series of slopes at both HH and HV-channel from the differencing method for L-band level (a) and deformed (b) ice, and C-band level (c) and deformed (d) ice. The dashed-dotted lines indicate a warming event (see Fig. 2). Note the difference in the y-axis for L and C-band. This is due to the presence of a significant amount of positive slopes for C-band level ice.

Time-series of the slopes for both level and deformed ice are shown in Figure 5, with the average slopes presented in Table 5. A brief warming event is highlighted by dashed-dotted lines

**Table 5.** Observed IA dependencies [dB / 1°] from L and C-band for level and deformed ice for the winter, melt onset and advanced melt seasons using the differencing method (*n* denotes the number of slope estimates used to calculate the statistics)

Wavelength	Ice type	Channel	Mean	SD	<i>n</i>	Season
L-band	Level	HH	-0.193	0.086	76	Winter
		HV	-0.055	0.081		
	Deformed	HH	-0.210	0.058	76	
		HV	-0.201	0.078		
C-band	Level	HH	-0.228	0.141	88	Winter
		HV	-0.045	0.175		
	Deformed	HH	-0.165	0.082	78	
		HV	-0.082	0.049		
L-band	Level	HH	-0.201	0.101	12	Melt onset
		HV	-0.112	0.097		
	Deformed	HH	-0.237	0.045	12	
		HV	-0.229	0.035		
C-band	Level	HH	-0.181	0.035	16	Melt onset
		HV	-0.069	0.194		
	Deformed	HH	-0.150	0.022	14	
		HV	-0.055	0.031		
L-band	Level	HH	-0.155	0.126	16	Advanced melt
		HV	-0.159	0.144		
	Deformed	HH	-0.180	0.053	16	
		HV	-0.206	0.083		
C-band	Level	HH	-0.308	0.144	6	Advanced melt
		HV	-0.209	0.096		
	Deformed	HH	-0.309	0.130	6	
		HV	-0.112	0.050		

(see section ‘Definition of seasons’), where a slight decrease in backscatter intensity for C-band deformed ice was observed. We therefore estimated the IA dependency using only winter season scenes acquired after the warming event, as well as all the scenes from the winter season and no significant difference was observable. We therefore chose to include all scenes from the winter season in the final slope estimates. We observe seasonal changes in the backscatter at both L and C-band (Figs 6, 7), highlighting the importance to separate the seasons when estimating the IA dependency. Though not as pronounced as the changes in backscatter, the IA dependency itself also has a seasonal variability, and is dependent on the frequency used and the different ice types observed (see Table 5).

During the winter season, we observe a stronger IA dependency in the co-polarized channel than in the cross-polarized channel at both L and C-band, though the difference is smaller for deformed ice at L-band. For the HH-channel, the IA dependency is similar for level and deformed ice at L-band, whereas there is a larger separation in the C-band data. For the HV-channel, the opposite is observed.

Previous L-band IA dependencies for sea ice have been focused on the HH-channel during wintertime (Mahmud and others, 2018; Karvonen and others, 2020; Singha and others, 2020; Toyota and others, 2021). In Mahmud and others (2018), slopes were estimated for FYI and MYI, which we assume are similar to our ice type definitions of level and deformed ice (see section on ‘Selection of ROIs’), as well as a general sea-ice slope, while the remaining studies only estimated general sea-ice slopes. The results from Mahmud and others (2018) (Table 1) are comparable to our findings for the FYI/level ice, though the



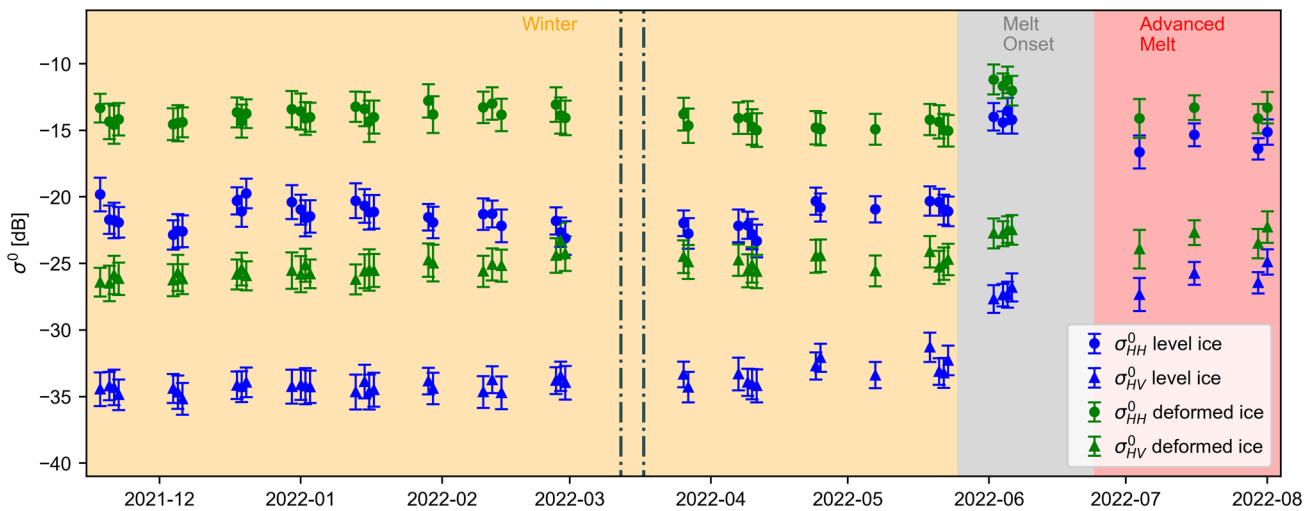


**Figure 6.** IA corrected L-band backscatter time-series projected to  $IA = 30^\circ$ . The dashed-dotted line indicates a warming event that occurred (see Fig. 2).

MYI slope was significantly steeper than the slope we retrieved for deformed ice. The unspecified HH-channel sea-ice slopes from Mahmud and others (2018); Karvonen and others (2020); Singha and others (2020) were approximately  $-0.25 \text{ dB/1}^\circ$ , which is steeper than both our level and deformed ice slopes.

Sea-ice IA dependency at C-band during the winter season has been well studied, particularly for the HH-channel, and for a range of different sea-ice areas (Mäkynen and Karvonen, 2017; Mahmud and others, 2018; Park and others, 2020; Geldsetzer and Howell, 2023). The slope estimates from these studies correspond well with our HH-channel slope estimates, apart from the HH-channel slope for deformed ice in Mäkynen and Karvonen (2017) ( $-0.24 \text{ dB/1}^\circ$ ), which is steeper than our slope estimate ( $-0.165 \text{ dB/1}^\circ$ ). Mäkynen and Karvonen (2017) also estimated HV-channel slopes for the winter season (level FYI:  $-0.23 \text{ dB/1}^\circ$ , deformed FYI:  $-0.16 \text{ dB/1}^\circ$ ), which were significantly steeper than our estimates (level ice:  $-0.045 \text{ dB/1}^\circ$ , deformed ice:  $-0.082 \text{ dB/1}^\circ$ ), though they expressed lower confidence in this estimate, due to noise contamination in the data and subsequently low signal-to-noise ratio.

We observe that the HV-channel backscatter is close to or below the system noise floor of both ALOS-2 and S1 for all seasons, with the winter season backscatter from level ice being well below the noise floor at both sensors. This might be the

cause of the large spread seen in the C-band HV-channel slope estimates for level ice (Fig. 5). In general, the HV-channel slope estimates also have a larger SD (Table 5), indicating that they are less precise and reliable than the HH estimates.

During melt onset, the L-band slopes increase slightly in steepness from the winter season (Table 5). This is more pronounced for the level ice HV-channel slope. For the advanced melt season, all slopes except the HV-channel level ice slope are shallower than during melt onset. To our knowledge, no previous separate L-band slope estimates for the melt season exist, though Karvonen and others (2020) estimated general sea-ice slopes for both the HH and HV-channel ( $-0.246$  and  $0.085 \text{ dB/1}^\circ$  respectively) for the period January–August. The HH-channel slope of Karvonen and others (2020) is steeper than both our level and deformed ice HH-channel slopes, while their HV-channel slope is significantly shallower than our HV-channel slope estimates. The latter result may have been affected by the change in processing of the HV-channel that was applied on 11 April 2018 by JAXA ([https://www.eorc.jaxa.jp/ALOS/en/alos-2/pdf/PALSAR2\\_ScanSAR\\_ATT\\_change\\_201808.pdf](https://www.eorc.jaxa.jp/ALOS/en/alos-2/pdf/PALSAR2_ScanSAR_ATT_change_201808.pdf), accessed 21 June 2024). Moreover, their estimates encompassed all of our seasons, which we observed had a large impact on the estimates.

For melt onset, our C-band slopes are comparable to the winter season slopes though slightly shallower. There is an increase in

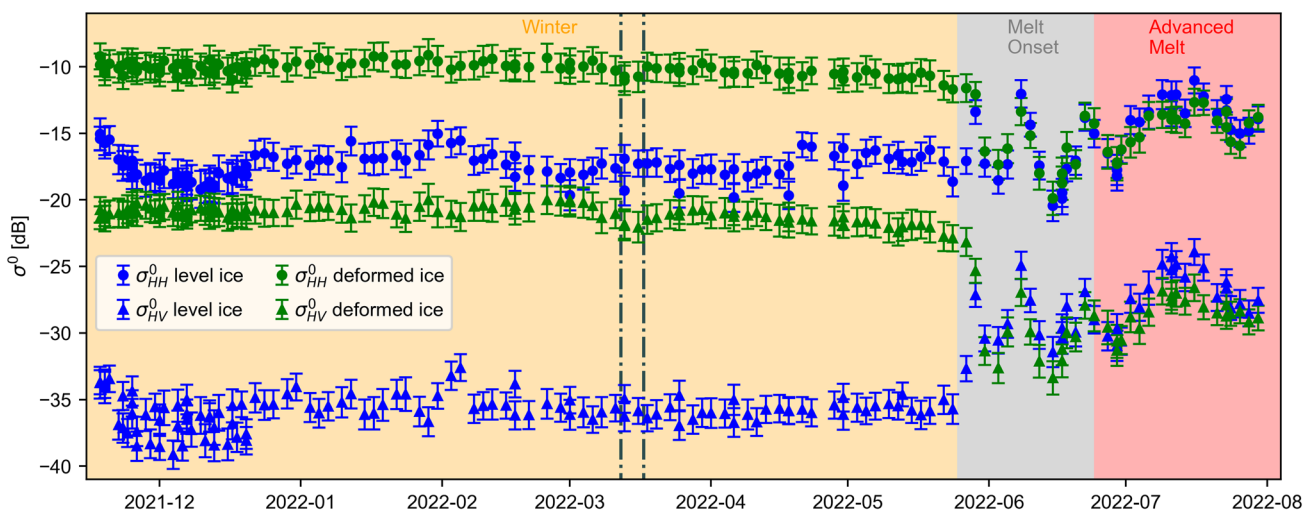


**Figure 7.** IA corrected C-band backscatter time-series projected to  $IA = 30^\circ$ . The dashed-dotted line indicates a warming event that occurred (see Fig. 2).



the spread of the HV-channel level ice slopes during the transition from winter to melt onset (Fig. 5). Geldsetzer and Howell (2023) also derived C-band slopes during melt onset (referred to as snowmelt in their study) and found them to be similar to the winter season slopes for FYI ( $-0.235 \text{ dB/1}^\circ$  for both seasons), while the slope estimates for SYI and MYI were steeper than the winter season slopes ( $-0.208 \text{ dB/1}^\circ$  and  $-0.167 \text{ dB/1}^\circ$  during winter,  $-0.241 \text{ dB/1}^\circ$  and  $-0.240 \text{ dB/1}^\circ$  during snowmelt, respectively). They also reported higher variability in the slope estimates from snowmelt compared to the winter season. The slopes from Mäkynen and Karvonen (2017) estimated from images acquired in the period 20 May 2016 and 17 June 2016 (deformed FYI HH:  $-0.26 \text{ dB/1}^\circ$ , deformed FYI HV:  $-0.18 \text{ dB/1}^\circ$ ) were also for this period significantly steeper than ours. Due to a small amount of data points, narrow range of  $\Delta \text{IA}$  and large spread in the data, they did not estimate the IA dependency for level ice during this period.

For C-band, all our slopes are significantly steeper during the advanced melt season than during melt onset. The slope estimates from the advanced melt season from Geldsetzer and Howell (2023) correspond well to our HH-channel slopes estimates, and are to our knowledge the only other source of advanced melt season estimates for C-band. It should be noted that the time separation for the L-band scenes from the advanced melt season varies from 1 to 14 days. This results in fewer available data points to estimate the IA dependency at L-band during the advanced melt season. The number of viable slopes (slopes with  $\Delta \bar{\text{IA}} > \Delta \bar{\text{IA}}_{\text{cutoff}}$ ) was also low for C-band during this season, with only six data points available.

Overall, our results show that there is seasonality in the IA dependency at both L and C-band that should be accounted for when analyzing SAR data over sea ice. Furthermore, we find that also the L-band HV-channel shows significant dependence on IA for both ice types in all three seasons. Hence, also L-band HV-channel data should be corrected for IA effects before further analysis.

#### 4.2 Analysis of temporal backscatter evolution

The IA corrected backscatter time-series (averaged for all ROIs) of level and deformed ice at both L and C-band, projected to  $\text{IA} = 30^\circ$ , are shown in Figures 6 and 7, respectively. For both frequencies, level and deformed ice is easily separable at  $\text{IA} = 30^\circ$  during the winter season. For the early part of the winter season (i.e. mid November to late December) a gradual decrease in the HH-channel level ice backscatter is observed at both L and C-band. For the C-band HV-channel, there is increased spread in the level ice backscatter during this period. This coincides with a period of increased spread in the HV-channel level ice slope estimates from C-band, while no visible effect is seen for the L-band slopes (Fig. 5). We attribute these effects to frost flow-ers on thin ice, where the initial backscatter is strong, but decreases with increasing sea ice thickness until a stable value for thick level ice is reached (Carsey, 1992). Following the freeze-up period, the backscatter for both ice types remains stable during the winter season at both frequencies, though the C-band level ice backscatter is more variable than the deformed ice backscatter. As the snow is cold and dry in this period, we assume that it is transparent for both the L and C-band radar signals. The main scattering mechanisms are therefore the same at both frequencies, though they are sensitive to roughness on different scales. For level ice, the backscatter is mainly surface scattering from the snow-ice interface, though some volume scattering from within the ice may be present. The latter effect is expected to be more pronounced at L-band, due to greater penetration depth. For deformed ice, the main scattering contribution is depolarization from the large-scale topography of the ice.

A brief warming period occurred between 12 March 2022 and 17 March 2022, where the air temperatures at Station Nord approached  $0^\circ \text{ C}$  (Fig. 2). During this period, a slight dip in backscatter intensity is observed for C-band deformed ice. This did not seem to have a notable impact on the slope estimates however, and as such we chose not to discard the data from this period. No L-band data were available for this period, and the impact of the warming event could therefore not be evaluated for this wavelength. The C-band backscatter also shows a transition period between winter and melt onset, where the deformed ice backscatter intensity gradually decreases, which we speculate could be associated with the early melt season. No such transition was observed at L-band.

As the ice transitions from the winter season to melt onset, an increase in backscatter is observed for both level and deformed ice at L-band, with increases in the average backscatter of approximately seven and three dB respectively at both the HH and HV-channel. Mahmud and others (2020) found that both FYI and MYI L-band SAR backscatter increased during melt onset, which they attributed to a combination of surface scattering from the ice-snow interface and volume scattering from the wet snow. A similar effect was observed by Ketchum Jr (1984) who attributed the increased backscatter to volume scattering from water-saturated snow or ice layers. According to Carsey (1992), longer wavelengths (such as L-band) would also be sensitive to superimposed ice at the snow-ice interface, which could also be a contributing factor depending on the wetness and thickness of the snow pack. For the deformed ice, we hypothesize that the signal is a combination of volume scattering from the wet snow and the large-scale topography of the sea ice. Hence, the deformed ice backscatter is stronger than the level ice backscatter. As such, the ice types remain separable at L-band during the melt onset season. The timing of the observed increase in backscatter corresponds well with the start of persisting positive temperatures from the SIMBA temperature measurements (Fig. 2). At C-band, the backscatter for deformed ice decreases during the transition from winter to melt onset, while a slight increase is observed for level ice. We attribute this to scattering from the wet snow being the dominant scattering source for both ice types, as the shorter wavelength is not able to penetrate the snow pack. The spread of backscatter values also increases for both classes, likely a result of the rapid changes occurring in the snow pack. This results in overlapping backscatter signatures for the two classes, making class separation practically impossible at C-band during the melt onset season.

During the advanced melt season, the L-band backscatter decreases for level and deformed ice at the HH-channel, and for deformed ice in the HV-channel. The level ice backscatter at HV remains consistent from the melt onset season. The deformed ice backscatter during this season is on a similar level as the backscatter during the winter season, while the level ice backscatter remains higher than during the winter season. We speculate that the amount of backscatter from the snow is reduced during this period, due to rapid melting of the snow pack. As such, the volume scattering contribution from the snow is reduced. Given the increased penetration depth of L-band, the signal is therefore dominated by scattering at the ice-snow interface and volume scattering from the internal structure of the ice and large-scale topography. The formation of melt ponds will likely also influence the SAR backscatter, though without ancillary wind data it is difficult to estimate their contribution. For C-band, an increase in backscatter is seen for both channels, which peaks around mid-July before a decrease with a similar rate is observed at both classes. A similar backscatter signature during the advanced melt season was observed by Barber and others (2001). We speculate that the increase in backscatter is caused by a reduction in the

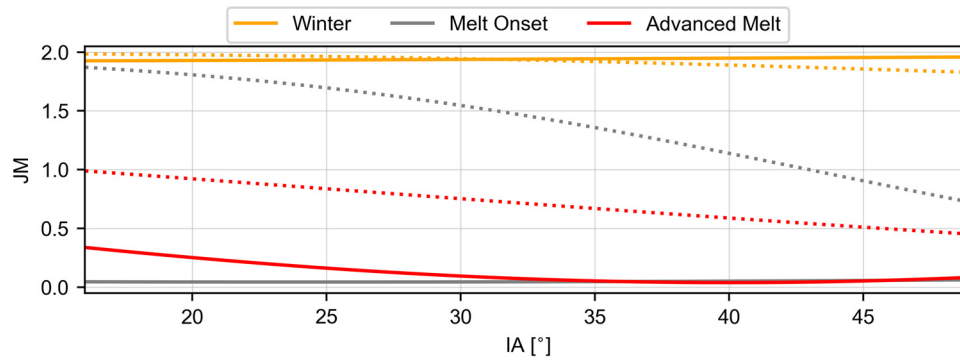


**Figure 8.** JM distance as a function of IA for L-band (dotted lines) and C-band (solid lines) for all seasons.

snow cover, causing the ice surface to be the dominant scattering source. As the ice surface is likely rougher during this stage of the season compared to the winter season due to superimposed ice, it has a stronger backscatter response than previously. The decrease in backscatter appears to persist throughout the end of the time-series for the landfast ice, which we attribute to surface melting and subsequent smoothing of the ice surface. However, due to the lack of in-situ data, it is impossible to confirm the exact processes of the backscatter evolution during this time period.

### 4.3 Class separability

We evaluated the class separability at both L and C-band for all seasons using the JM-distance. The class separability as a function of IA for the range  $IA \in (15^\circ, 50^\circ)$  is shown in Figure 8, while the class distributions for the backscatter projected to  $IA = 30^\circ$  and

corresponding JM distance are presented in Figure 9. The class separability remains consistently high during the winter season at both L and C-band for the range of IAs investigated, with the L-band separability slightly decreasing with increasing IA and the C-band separability slightly increasing as a function of IA. As the IA range encompasses the IA range of both ALOS-2 ScanSAR and S1 EW (Table 2), the separability remains high across the width of the SAR imagery evaluated in this study. For both L and C-band, the ice types are well separable in both the HH and HV-channel during the winter season (Fig. 9).

For L-band, the class separability decreases with increasing IA for both the melt onset and advanced melt seasons. The separability at L-band transitions from high to low separability ( $JM < 1$ ) around  $IA = 42^\circ$  and  $IA = 15^\circ$  for the melt onset and advanced melt seasons, respectively. The class separability at C-band during the melt onset and advanced melt seasons is low for the range of

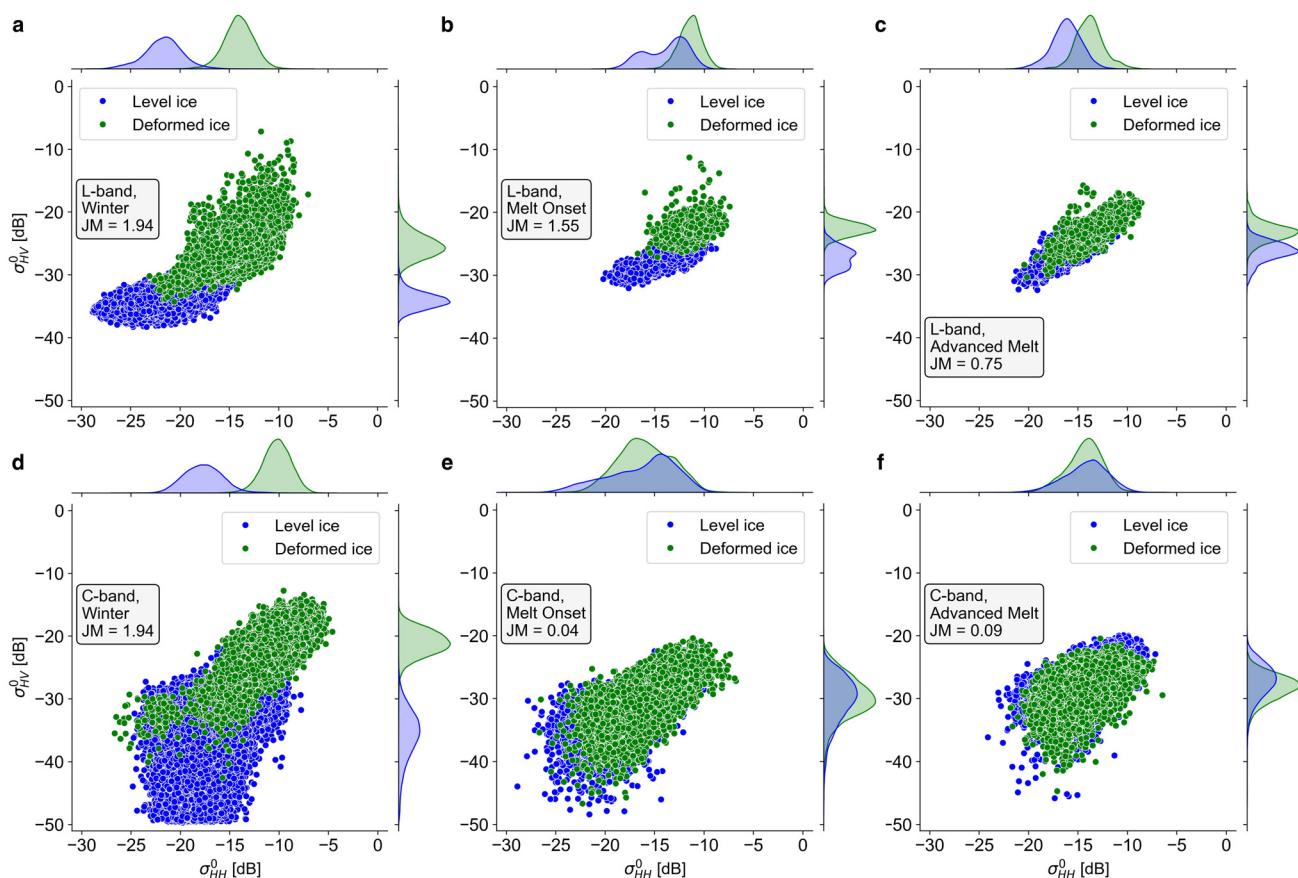


**Figure 9.** Joint plots of L and C-band backscatter distributions projected to  $IA = 30^\circ$  for level and deformed ice with the JM distance included as a measure of separability. (a–c) L-band distributions for winter, melt onset and advanced melt. (d–f) C-band distributions for winter, melt onset and advanced melt.

IAs investigated. The possibility of using L-band SAR during melt onset is in line with what was observed by Casey and others (2016), where they found that the separability of FYI and MYI for the L-band HH-channel was similar during winter and melt onset, while the separability at the C-band HH-channel was greatly reduced during melt onset.

At L-band the classes have high separability during the winter and melt onset seasons and the cross-polarized channel appears to be the most important for separating the classes during the melt onset season. We observe that the HV-channel signal in particular from level ice is significantly stronger during melt onset compared to the winter season. This makes interpretation and classification based on the HV-channel more reliable during melt onset, as the influence of thermal system noise is reduced. Since the HV-channel backscatter from deformed ice is well above the level ice signal, we can still use the HV-channel to reliably separate the two ice types until the transition to the advanced melt season.

The C-band backscatter during the advanced melt season follows a parabolic trend, with a peak around mid-July (Fig. 7). This

peak coincides with a transition in the SIMBA temperature profile, from around 0 to above 0° C (Fig. 2), indicating a transition to significant snow and/or ice melt. While the HH-channel backscatter intensity for level and deformed ice during advanced melt is roughly equal in strength, the HV-channel level ice backscatter is slightly stronger than the deformed ice backscatter. However, the difference is very small and insufficient for clear class separation, as is indicated by the still relatively low separability score for C-band during advanced melt (Fig. 8).

#### 4.4 Classification

Here we present the classification results from both L and C-band imagery. Example ice type maps retrieved from both frequencies are shown in Figure 10, together with the corresponding HH-channel backscatter images. For this example, both frequencies produce similar results, showing almost identical spatial distribution of level and deformed ice.

The performance of the classifiers was evaluated on scenes from the 2022–2023 season, independent of the training data

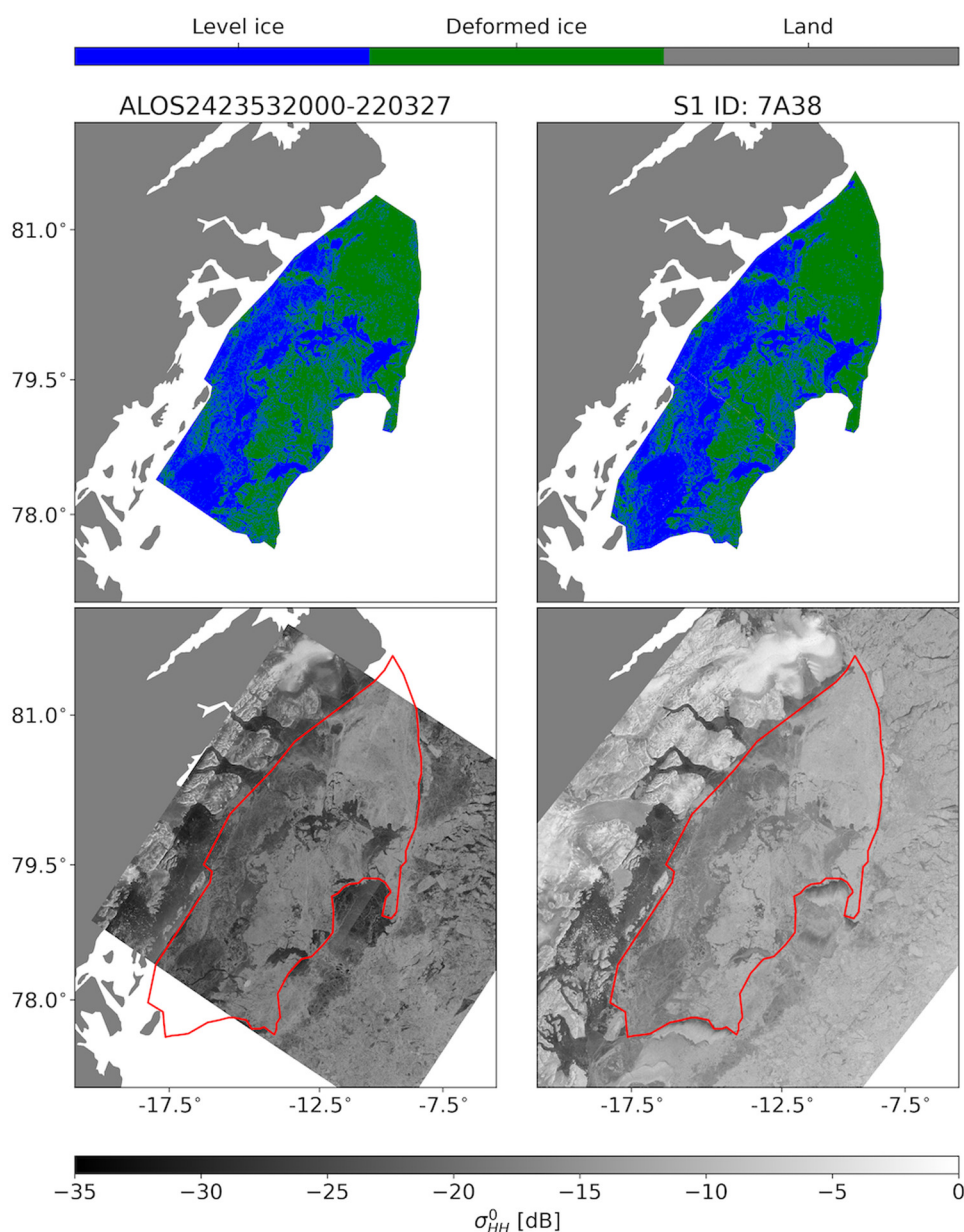


**Figure 10.** Comparison between classification results from L and C-band, as well as the respective HH-channel backscatter images. The images were acquired during the winter season (ALOS-2: 27 March 2022, S1: 28 March 2022). The red line indicates the fast ice edge.



**Table 6.** Classification accuracies for the 2023 data at both L and C-band ( $n_l$  and  $n_d$  denotes the number of pixels used for evaluating performance from each scene for level and deformed ice respectively)

Wavelength	Scene ID	Per-class accuracy and pixel count				OA	Season
		Level ice	$n_l$	Deformed ice	$n_d$		
L-band	ALOS2475432000-230313	83.7%	1756	99.7%	1768	91.7%	Winter
	ALOS2479572000-230410	96.0%	1732	97.9%	1656	96.9%	
	ALOS2483712000-230508	95.9%	1768	98.3%	1732	97.1%	
C-band	20230313 4AE4	85.8%	1755	99.1%	1695	92.3%	Winter
	20230411 DB4B + E1F1	99.9%	1782	98.8%	1730	99.4%	
L-band	20230508 DA6C	100%	1731	98.6%	1781	99.3%	Melt
	ALOS2487702000-230604	100%	1770	71.6%	1755	85.8%	
C-band	ALOS2487852000-230605	97.2%	1692	88.0%	1719	92.6%	Onset
	20230603 C171 + 2C2F	57.9%	1782	31.4%	1730	44.8%	
L-band	20230605 B85B	59.2%	1695	34.7%	1743	46.8%	Advanced Melt
C-band	ALOS2491992000-230703	51.8%	1730	97.3%	1669	74.2%	
C-band	20230704 5E3C	69.3%	1706	65.5%	1757	67.4%	Melt

from the 2021–2022 season. Test accuracies are presented in Table 6. While both frequencies achieve high OA during the winter season ( $> 90\%$ ), the L-band classifier performs significantly better than the C-band classifier during the melt onset period (85.8 and 92.6% on two separate images for L-band versus 44.8 and 46.8% for the two corresponding images at C-band). During the advanced melt season both frequencies achieve similar results (L-band: 74.2%, C-band: 67.4%).

Looking at the per-class accuracies for L-band, both level and deformed ice accuracy was high during the winter season, with all scores except one (level ice on 13 March 2023) above 95%. During the melt onset season, the level ice accuracy remained high, but the deformed ice accuracy dropped significantly. This trend was reversed during the advanced melt season, where the classification accuracy for deformed ice was significantly higher than for level ice.

For C-band, a similar trend was observed during the winter season, with high per-class accuracies overall except for level ice on 13 March 2023. During the melt onset season, the per-class accuracy was higher for level ice than for deformed ice, though both classes had low accuracy. For the advanced melt season, per-class accuracy for level and deformed ice were similar, but still lower than during the winter season.

While the OAs for L and C-band are similar during the advanced melt season, the per-class accuracies differ significantly. For L-band, the deformed ice accuracy is high while the level ice accuracy is low. This indicates a bias toward deformed ice for the L-band classifier. For C-band, the per-class accuracies are similarly low for level and deformed ice, and the OA is slightly lower than for L-band. Both wavelengths therefore show limitations during the advanced melt season.

As expected, the classification accuracies correspond well with the separability scores (Fig. 8), with high separability and classification accuracy during the winter season at both L and C-band and during the melt onset season at L-band, moderately high separability and classification accuracies for both frequencies during the advanced melt season, and low classification accuracies and separability for C-band during the melt onset season. The C-band OA was only slightly lower than the L-band OA during the advanced melt season, despite the JM distance being significantly lower for C-band ( $JM < 0.5$  at C-band for all IAs, while  $JM \in (0.5, 1)$  for L-band).

## 5. Conclusion

From time-series of L and C-band SAR data spanning the winter, melt onset and advanced melt seasons, we estimated IA dependencies for level and deformed ice for both the HH and HV-channel. We show that the IA dependency at both frequencies is dependent on season, ice type and polarization channel, which has not previously been investigated for L-band. The IA

dependencies are used to radiometrically correct the backscatter time-series, allowing for more detailed analysis of the temporal evolution. We observe that while the level and deformed ice backscatter is indistinguishable at C-band during melt onset, the classes remain well separable at L-band, with both ice types showing an increase in backscatter intensity during this period. During the advanced melt season, both frequencies show limited capability in separating level and deformed ice. Furthermore, the L-band time series during this period is sparse with a lower temporal resolution, which leads to less reliable slope estimates and in turn affects the assessment of class separability. Accurate separation of level and deformed ice well into the melt season is of importance for operational ice mapping, as deformed ice poses a significant challenge for marine operations. Finally, we use our findings to train an IA aware Bayesian classifier at both L and C-band, taking seasonality into account. The test accuracies align with what we would expect from the class separability, with high classification accuracy during the winter season at both frequencies, high classification accuracy during melt onset at L-band and low accuracy for C-band, and moderately high classification accuracy for both L and C-band during the advanced melt season. While our study is limited to fast ice in the Belgica Bank area, we expect that the overall findings on level-versus-deformed ice separability are transferable to drift ice with similar large-scale deformation features, such as for example drift ice in Fram Strait. However, comparison and transferability to studies from other regions such as the Canadian Arctic is more challenging due to differences in large-scale deformation, as well as a mixture of FYI and MYI within the deformed ice class of our study. Nevertheless, our results highlight the importance of seasonal and IA effects on L-band radar backscatter from different sea-ice types and demonstrate the capabilities of L-band SAR for operational ice type mapping, which is of interest given several upcoming L-band SAR missions such as NISAR, ALOS-4 and ROSE-L.

**Acknowledgements.** This research was funded by the Research Council of Norway through the project Center for Integrated Remote Sensing and Forecasting for Arctic Operations (CIRFA) (grant number 237 906), and the European Space Agency through RFP Response No 3-17845. The ALOS-2 PALSAR-2 scenes were provided by JAXA under the 3rd Research Announcement on Earth Observations (PI: Malin Johansson PER3A2N093). The presented work contains primary and altered Sentinel data products (@Copernicus data).

## References

- Aldenhoff W, Heuzé C and Eriksson LE (2018) Comparison of ice/water classification in Fram Strait from C-and L-band SAR imagery. *Annals of Glaciology* 59(76pt2), 112–123. doi: [10.1017/aog.2018.7](https://doi.org/10.1017/aog.2018.7)



- Aldenhoff W, Eriksson LE, Ye Y and Heuzé C (2020) First-year and multi-year sea ice incidence angle normalization of dual-polarized Sentinel-1 SAR images in the Beaufort Sea. *IEEE Journal of Selected Topics in Applied Earth Observations and Remote Sensing* **13**, 1540–1550. doi: [10.1109/JSTARS.2020.2977506](https://doi.org/10.1109/JSTARS.2020.2977506)
- Barber DG, Yackel J and Hanesiak J (2001) Sea ice, RADARSAT-1 and Arctic climate processes: a review and update. *Canadian Journal of Remote Sensing* **27**(1), 51–61. doi: [10.1080/07038992.2001.10854919](https://doi.org/10.1080/07038992.2001.10854919)
- Carsey FD (1992) *Microwave Remote Sensing of Sea Ice*. Washington, DC: American Geophysical Union.
- Casey JA, Howell SE, Tivy A and Haas C (2016) Separability of sea ice types from wide swath C-and L-band synthetic aperture radar imagery acquired during the melt season. *Remote sensing of environment* **174**, 314–328. doi: [10.1016/j.rse.2015.12.021](https://doi.org/10.1016/j.rse.2015.12.021)
- Cristea A, Van Houtte J and Doulgeris AP (2020) Integrating incidence angle dependencies into the clustering-based segmentation of SAR images. *IEEE Journal of Selected Topics in Applied Earth Observations and Remote Sensing* **13**, 2925–2939. doi: [10.1109/JSTARS.2020.2993067](https://doi.org/10.1109/JSTARS.2020.2993067)
- Dabboor M, Montpetit B, Howell S and Haas C (2017) Improving sea ice characterization in dry ice winter conditions using polarimetric parameters from C-and L-band SAR data. *Remote Sensing* **9**(12), 1270. doi: [10.3390/rs9121270](https://doi.org/10.3390/rs9121270)
- Dierking W (2009) Mapping of different sea ice regimes using images from Sentinel-1 and ALOS synthetic aperture radar. *IEEE Transactions on Geoscience and Remote Sensing* **48**(3), 1045–1058. doi: [10.1109/TGRS.2009.2031806](https://doi.org/10.1109/TGRS.2009.2031806)
- Dierking WFO, Schneider A, Eltoft T and Gerland S (2022) CIRFA Cruise 2022. Cruise report. UiT, Department of Physics and Technology, 123.
- Færch L, Dierking W, Hughes N and Doulgeris AP (2024) Mapping icebergs in sea ice: an analysis of seasonal SAR backscatter at C-and L-band. *Remote Sensing of Environment* **304**, 114074. doi: [10.1016/j.rse.2024.114074](https://doi.org/10.1016/j.rse.2024.114074)
- Geldsetzer T and Howell SE (2023) Incidence angle dependencies for C-band backscatter from sea ice during both the winter and melt season. *IEEE Transactions on Geoscience and Remote Sensing* **61**, 1–15. doi: [10.1109/TGRS.2023.3315056](https://doi.org/10.1109/TGRS.2023.3315056)
- Hughes NE, Wilkinson JP and Wadhams P (2011) Multi-satellite sensor analysis of fast-ice development in the Norske Øer Ice Barrier, northeast Greenland. *Annals of Glaciology* **52**(57), 151–160. doi: [10.3189/172756411795931633](https://doi.org/10.3189/172756411795931633)
- Jackson K and 6 others (2013) A novel and low-cost sea ice mass balance buoy. *Journal of Atmospheric and Oceanic Technology* **30**(11), 2676–2688. doi: [10.1175/JTECH-D-13-00058.1](https://doi.org/10.1175/JTECH-D-13-00058.1)
- Karvonen J, Rinne E, Sallila H and Mäkynen M (2020) On suitability of ALOS-2/PALSAR-2 dual-polarized SAR data for Arctic sea ice parameter estimation. *IEEE Transactions on Geoscience and Remote Sensing* **58**(11), 7969–7981. doi: [10.1109/TGRS.2020.2985696](https://doi.org/10.1109/TGRS.2020.2985696)
- Ketchum Jr R (1984) SEASAT SAR sea-ice imagery: summer melt to autumn freeze-up. *Remote Sensing* **5**(3), 533–544. doi: [10.1080/01431168408948834](https://doi.org/10.1080/01431168408948834)
- Lasserre F and Pelletier S (2011) Polar super seaways? Maritime transport in the Arctic: an analysis of shipowners' intentions. *Journal of Transport Geography* **19**(6), 1465–1473. doi: [10.1016/j.jtrangeo.2011.08.006](https://doi.org/10.1016/j.jtrangeo.2011.08.006)
- Lasserre F and Têtu PL (2020) Transportation in the melting Arctic: contrasting views of shipping and railway development. *Cahiers de l'Institut EDS* **37**, 6–16.
- Lohse J, Doulgeris AP and Dierking W (2020) Mapping sea-ice types from Sentinel-1 considering the surface-type dependent effect of incidence angle. *Annals of Glaciology* **61**(83), 260–270. doi: [10.1017/aog.2020.45](https://doi.org/10.1017/aog.2020.45)
- Lohse J, Taelman C, Everett A and Hughes N (2024) Automated Sentinel-1 ice type mapping and in-situ validation during the CIRFA-22 cruise. *Annals of Glaciology* 1–28. doi: [10.1017/aog.2024.23](https://doi.org/10.1017/aog.2024.23)
- Mahmud MS and 5 others (2018) Incidence angle dependence of HH-polarized C-and L-band wintertime backscatter over Arctic sea ice. *IEEE Transactions on Geoscience and Remote Sensing* **56**(11), 6686–6698. doi: [10.1109/TGRS.2018.2841343](https://doi.org/10.1109/TGRS.2018.2841343)
- Mahmud MS, Nandan V, Howell SE, Geldsetzer T and Yackel J (2020) Seasonal evolution of L-band SAR backscatter over landfast Arctic sea ice. *Remote Sensing of Environment* **251**, 112049. doi: [10.1016/j.rse.2020.112049](https://doi.org/10.1016/j.rse.2020.112049)
- Mahmud MS and 6 others (2022) C- and L-band SAR signatures of Arctic sea ice during freeze-up. *Remote Sensing of Environment* **279**, 113129. doi: [10.1016/j.rse.2022.113129](https://doi.org/10.1016/j.rse.2022.113129)
- Mäkynen M and Karvonen J (2017) Incidence angle dependence of first-year sea ice backscattering coefficient in Sentinel-1 SAR imagery over the Kara Sea. *IEEE Transactions on Geoscience and Remote Sensing* **55**(11), 6170–6181. doi: [10.1109/TGRS.2017.2721981](https://doi.org/10.1109/TGRS.2017.2721981)
- Mäkynen M, Manninen AT, Similä M, Karvonen JA and Hallikainen MT (2002) Incidence angle dependence of the statistical properties of C-band HH-polarization backscattering signatures of the Baltic Sea ice. *IEEE Transactions on Geoscience and Remote Sensing* **40**(12), 2593–2605. doi: [10.1109/TGRS.2002.806991](https://doi.org/10.1109/TGRS.2002.806991)
- Malmgren-Hansen D and 8 others (2020) A convolutional neural network architecture for Sentinel-1 and AMSR2 data fusion. *IEEE Transactions on Geoscience and Remote Sensing* **59**(3), 1890–1902. doi: [10.1109/TGRS.2020.3004539](https://doi.org/10.1109/TGRS.2020.3004539)
- Meier WN and Stroeve J (2022) An updated assessment of the changing Arctic sea ice cover. *Oceanography* **35**(3/4), 10–19. doi: [10.5670/oceanog.2022.114](https://doi.org/10.5670/oceanog.2022.114)
- Onstott RG and Carsey F (1992) SAR and scatterometer signatures of sea ice. *Microwave remote sensing of sea ice* **68**, 73–104.
- Park JW and 5 others (2020) Classification of sea ice types in Sentinel-1 synthetic aperture radar images. *The Cryosphere* **14**(8), 2629–2645. doi: [10.5194/tc-14-2629-2020](https://doi.org/10.5194/tc-14-2629-2020)
- Sen R, Goswami S and Chakraborty B (2019) Jeffries-Matusita distance as a tool for feature selection. In *2019 International Conference on Data Science and Engineering (ICDSE)*, 15–20, IEEE. doi: [10.1109/ICDSE47409.2019.8971800](https://doi.org/10.1109/ICDSE47409.2019.8971800)
- Singha S, Johansson AM and Doulgeris AP (2020) Robustness of SAR sea ice type classification across incidence angles and seasons at L-band. *IEEE Transactions on Geoscience and Remote Sensing* **59**(12), 9941–9952. doi: [10.1109/TGRS.2020.3035029](https://doi.org/10.1109/TGRS.2020.3035029)
- Stehman SV, Foody GM (2009) *The SAGE handbook of remote sensing*. Sage Publications Ltd, London, United Kingdom.
- Stephenson SR, Smith LC, Brigham LW and Agnew JA (2013) Projected 21st-century changes to Arctic marine access. *Climatic Change* **118**, 885–899. doi: [10.1007/s10584-012-0685-0](https://doi.org/10.1007/s10584-012-0685-0)
- Toyota T, Ishiyama J and Kimura N (2021) Measuring deformed sea ice in seasonal ice zones using L-band SAR images. *IEEE Transactions on Geoscience and Remote Sensing* **59**(11), 9361–9381. doi: [10.1109/TGRS.2020.3043335](https://doi.org/10.1109/TGRS.2020.3043335)
- Vinje T (1986) The ice transport through the Fram Strait. *Polar Research* **4**, 81–89. doi: [10.1111/j.1751-8369.1986.tb00548.x](https://doi.org/10.1111/j.1751-8369.1986.tb00548.x)
- Wakabayashi H, Matsuoka T, Nakamura K and Nishio F (2004) Polarimetric characteristics of sea ice in the Sea of Okhotsk observed by airborne L-band SAR. *IEEE Transactions on Geoscience and Remote Sensing* **42**(11), 2412–2425. doi: [10.1109/TGRS.2004.836259](https://doi.org/10.1109/TGRS.2004.836259)
- Wang Q, Lohse J, Doulgeris AP and Eltoft T (2023) Data augmentation for SAR sea ice and water classification based on per-class backscatter variation with incidence angle. *IEEE Transactions on Geoscience and Remote Sensing* **61**, 1–15. doi: [10.1109/TGRS.2023.3291927](https://doi.org/10.1109/TGRS.2023.3291927)

## APPENDIX A

**Table 7.** Overview of ALOS-2 scenes used in the study

Scene ID			
ALOS2404462000-211118	ALOS2404752000-211120	ALOS2404902000-211121	ALOS2405052000-211122
ALOS2406822000-211204	ALOS2406972000-211205	ALOS2407122000-211206	ALOS2408892000-211218
ALOS2409042000-211219	ALOS2409192000-211220	ALOS2410672000-211230	ALOS2410962000-220101
ALOS2411112000-220102	ALOS2411262000-220103	ALOS2412742000-220113	ALOS2413032000-220115
ALOS2413182000-220116	ALOS2413332000-220117	ALOS2415102000-220129	ALOS2415252000-220130
ALOS2416882000-220210	ALOS2417172000-220212	ALOS2417472000-220214	ALOS2419242000-220226
ALOS2419392000-220227	ALOS2419542000-220228	ALOS2423382000-220326	ALOS2423532000-220327
ALOS2425162000-220407	ALOS2425452000-220409	ALOS2425602000-220410	ALOS2425752000-220411
ALOS2427672000-220424	ALOS2427822000-220425	ALOS2429592000-220507	ALOS2431372000-220519
ALOS2431662000-220521	ALOS2431812000-220522	ALOS2431962000-220523	ALOS2433442000-220602
ALOS2433732000-220604	ALOS2433882000-220605	ALOS2434032000-220606	ALOS2438172000-220704
ALOS2439942000-220716	ALOS2442012000-220730	ALOS2442312000-220801	ALOS2443562000-220805
ALOS2475432000-230313	ALOS2479572000-230410	ALOS2483712000-230508	ALOS2487552000-230603
ALOS2487852000-230605	ALOS2491992000-230703		